

# Segregation of Calcium and Magnesium into Different Substructures. $\text{Ca}_4\text{Ag}_{0.948}\text{Mg}$ and Other Compounds with $\text{Gd}_4\text{RhIn}$ -type Structure

Marcel Kersting<sup>a</sup>, Samir F. Matar<sup>b</sup>, Christian Schwickert<sup>a</sup>, and Rainer Pöttgen<sup>a</sup>

<sup>a</sup> Institut für Anorganische und Analytische Chemie, Universität Münster, Corrensstraße 30, 48149 Münster, Germany

<sup>b</sup> CNRS, Université de Bordeaux, ICMCB, 87 Avenue du Docteur Albert Schweitzer, 33600 Pessac, France

Reprint requests to R. Pöttgen. E-mail: pottgen@uni-muenster.de

*Z. Naturforsch.* **2012**, 67b, 61–69; received December 12, 2011

The metal-rich compounds  $R_4\text{PdMg}$  ( $R = \text{Ca}, \text{Eu}, \text{Tb–Lu}$ ),  $R_4\text{AgMg}$  ( $R = \text{Ca}, \text{Yb}$ ),  $R_4\text{PtMg}$  ( $R = \text{Eu}, \text{Tb–Lu}$ ), and  $R_4\text{AuMg}$  ( $R = \text{Ca}, \text{Eu}, \text{Yb}$ ) were synthesized by induction melting of the elements in sealed tantalum tubes in a water-cooled sample chamber. All samples were characterized by powder X-ray diffraction. The structures of  $\text{Ca}_4\text{Ag}_{0.948}\text{Mg}$  and  $\text{Yb}_4\text{PdMg}$  were refined on the basis of single-crystal X-ray diffractometer data:  $\text{Gd}_4\text{RhIn}$  type,  $F\bar{4}3m$ ,  $a = 1434.6(1)$  pm,  $wR2 = 0.0269$ , 523  $F^2$  values, 18 variables for  $\text{Yb}_4\text{PdMg}$  and  $a = 1485.78(7)$  pm,  $wR2 = 0.0188$ , 617  $F^2$  values, 20 variables for  $\text{Ca}_4\text{Ag}_{0.948}\text{Mg}$ . For the first time small defects on the  $16e$  transition metal site of a  $\text{Gd}_4\text{RhIn}$ -type compound have been observed, and the first compounds of this structure type with the divalent rare earth elements europium and ytterbium as well as with calcium are reported. The striking structural motif of these compounds (exemplary for  $\text{Ca}_4\text{Ag}_{0.948}\text{Mg}$ ) is the clear segregation of two alkaline earth elements into two different substructures, calcium forming trigonal prisms around the silver atoms and magnesium forming covalently bonded tetrahedra (Mg–Mg 328 pm). The latter are embedded in larger cavities of the adamantane-like three-dimensional network of edge- and corner-sharing  $\text{AgCa}_6$  trigonal prisms. This is evident from the chemical bonding analysis of the electronic structure by *ab initio* calculations. The density of states shows *s*-like metallic conductivity with an active role played by the Ag *d* states within the valence band and for the bonding with calcium. Temperature-dependent magnetic susceptibility data of  $\text{Eu}_4\text{PdMg}$  and  $\text{Eu}_4\text{PtMg}$  show Curie-Weiss behavior above 230 K with experimental magnetic moments of 7.94(1) and 8.00(1)  $\mu_B$  per Eu atom for the palladium and platinum compound, respectively. Ferromagnetic ordering is detected at the comparatively high Curie temperatures of 150.1(5) ( $\text{Eu}_4\text{PdMg}$ ) and 139.1(5) ( $\text{Eu}_4\text{PtMg}$ ) K. Magnetization measurements at 3 K show full parallel spin alignment and the typical behavior of soft ferromagnets.

**Key words:** Crystal Structure, Alkaline Earth Metals, Magnesium, Ferromagnetic Ordering

## Introduction

The cubic  $\text{Gd}_4\text{RhIn}$  structure type [1], space group  $F\bar{4}3m$ , has two striking structural motifs. The rhodium-centered  $\text{RhGd}_6$  trigonal prisms with strong covalent Gd–Rh bonding are condensed *via* common corners and edges to a three-dimensional adamantane-related network in which cavities are filled by  $\text{In}_4$  tetrahedra, a rare structural motif in main group chemistry. Besides the series of  $RE_4T\text{In}$  ( $RE = \text{rare earth metal}$ ;  $T = \text{Ru}, \text{Rh}, \text{Ir}$ ) indides [1–4], also many aluminides, as well as magnesium and cadmium compounds have been reported [4–6 and refs. therein]. Already 200 representatives of this structure type are known. The formation of covalently bonded  $\text{Mg}_4$  and  $\text{Cd}_4$  tetrahedra in

this peculiar structure type is a surprising feature and strongly underlines that magnesium does not behave like a typical alkaline earth element [7].

The stability range of such intermetallic structure types mostly extends over a small range of the valence electron concentration (VEC). The  $RE_4TX$  ( $T = \text{Co}, \text{Ni}, \text{Ru}, \text{Rh}, \text{Pd}, \text{Ir}, \text{Pt}$ ;  $X = \text{Mg}, \text{Al}, \text{In}, \text{Cd}$ ) series allow for small VEC changes through substitution on the *T* and *X* site enabling property modifications. Some of the  $RE_4TX$  intermetallics show promising chemical and physical properties. The  $4f^7$  system  $\text{Gd}_4\text{NiMg}$  [8] shows antiferromagnetic ordering at 92 K. The compound absorbs up to 11 hydrogen atoms per formula unit. Hydrogenation destroys the magnetic coupling, and  $\text{Gd}_4\text{NiMgH}_{11}$  remains para-

magnetic down to 1.8 K. Two further interesting compounds are the magnetocaloric material  $\text{Er}_4\text{NiCd}$  [9] and the solid solution  $\text{Gd}_4\text{NiMg}_{1-x}\text{Al}_x$  [10] which shows a switch from magnetic ordering to spin-glass behavior upon increasing magnesium substitution.

The  $\text{RE}_4\text{TX}$  compounds synthesized up to now all contained exclusively the trivalent rare earth elements. In continuation of our phase analytical work on the rare earth metal-rich  $\text{RE-T-Mg}$  systems we could complete the series of  $\text{RE}_4\text{PdMg}$  and  $\text{RE}_4\text{PtMg}$  compounds. So far only  $\text{RE}_4\text{PdMg}$  with  $\text{RE} = \text{Y, Sm, Gd}$  and  $\text{RE}_4\text{PtMg}$  with  $\text{RE} = \text{Y, Nd, Sm, Gd}$  had been reported [11]. For the first time it was now possible to synthesize  $\text{RE}_4\text{TX}$  compounds with the divalent rare earth elements europium and ytterbium. Given the comparable radii [12] of  $\text{Ca}^{2+}$  (106 pm) and  $\text{Yb}^{2+}$  (113 pm), as well as  $\text{Sr}^{2+}$  (127 pm) and  $\text{Eu}^{2+}$  (112 pm), we were also successful in the synthesis of isotypic calcium compounds  $\text{Ca}_4\text{TMg}$  ( $T = \text{Pd, Ag, Au}$ ) which show a distinct segregation of magnesium and calcium into different substructures. The synthesis, crystal and electronic structures, and some properties of these intermetallics are reported herein.

## Experimental Section

### Synthesis

Starting materials for the syntheses of the  $\text{R}_4\text{TMg}$  samples were distilled calcium granules (Johnson Matthey, > 99.5 %), ingots of the trivalent rare earth metals (smart elements, > 99.9 %), sublimed pieces of europium (Johnson Matthey, > 99.9 %), palladium and platinum powder (Degussa-Hüls, > 99.9 %), pieces of a gold bar (Heraeus, > 99.9 %), and a magnesium rod (Johnson Matthey,  $\varnothing$  16 mm, > 99.5 %; the surface of the rod was first cut on a turning lathe in order to remove surface impurities). Pieces of calcium or the rare earth elements, the noble metal powders or pieces and turnings of the magnesium rod were weighed in the ideal 4 : 1 : 1 atomic ratios and arc-welded [13] in small tantalum tubes under an argon pressure of *ca.* 800 mbar. The argon was purified over titanium sponge (900 K), silica gel, and molecular sieves. The sealed ampoules were placed in a water-cooled sample chamber [14] of a high-frequency furnace (Hüttinger Elektronik, Freiburg, type TIG 1.5/300) under flowing argon and first annealed at 1400 K for about 5 min, followed by cooling to 900 K within 50 min. Finally the samples were annealed for 2 h at that temperature, followed by quenching. The temperature was controlled through a Sensor Therm Methis MS09 pyrometer with an accuracy of  $\pm 30$  K. For the preparation of  $\text{Ca}_4\text{AgMg}$  the elements were also weighed in 4 : 1 : 1 ratio and arc-welded in a tantalum ampoule. The latter was sealed in a quartz tube for

oxidation protection and then annealed within 5 h to 1223 K in a muffle furnace. After keeping the temperature for 2 h it was lowered to 823 K within 24 h, kept at 823 K for another 10 h followed by radiative heat loss. The samples were separated mechanically from the ampoules. No reactions with the crucible material were evident. The polycrystalline  $\text{RE}_4\text{TMg}$  samples are stable in air, while the calcium-containing ones are sensitive to moisture and were kept in Schlenk tubes.

### EDX data

Semiquantitative EDX analyses of the single crystals studied on the diffractometer were carried out in variable pressure mode with a Zeiss EVO<sup>®</sup> MA10 scanning electron microscope with  $\text{CaSiO}_3$ ,  $\text{YbF}_3$ , Ag, Pd, and  $\text{MgO}$  as standards. The experimentally observed average compositions were close to the ideal ones. No impurity elements were detected.

### X-Ray diffraction

The powdered polycrystalline  $\text{Ca}_4\text{TMg}$  and  $\text{RE}_4\text{TMg}$  samples were characterized by Guinier patterns (imaging plate detector, Fujifilm BAS-1800) with  $\text{CuK}\alpha_1$  radiation and  $\alpha$ -quartz ( $a = 491.30$ ,  $c = 540.46$  pm) as an internal standard. The cubic lattice parameters (Table 1) were obtained from least-squares refinements. Correct indexing of the patterns was ensured through intensity calculations [15].

Small single crystals were selected from the crushed  $\text{Ca}_4\text{AgMg}$  and  $\text{Yb}_4\text{PdMg}$  samples, glued to quartz fibers using a two-component adhesive resin and studied on a Buerger camera (using white Mo radiation) to check their quality. Data sets of well-shaped crystals were collected in oscillation mode on a Stoe IPDS II diffractometer using  $\text{MoK}\alpha$  radiation. Numerical absorption corrections were applied to the data sets. Details about the data collections and the crystallographic parameters are summarized in Table 2.

### Structure refinements

Both diffractometer data sets showed face-centered cubic lattices and no further systematic extinction conditions. The non-centrosymmetric space group  $F\bar{4}3m$  was found to be correct in agreement with previous work on  $\text{RE}_4\text{TMg}$  [5] and  $\text{RE}_4\text{TCd}$  [6] intermetallics. The atomic parameters of  $\text{Gd}_4\text{PtMg}$  [11] were taken as starting values, and both structures were refined with anisotropic displacement parameters for all atoms with SHELXL-97 (full-matrix least-squares on  $F_o^2$ ) [16]. To check for deviations from the ideal compositions, the occupancy parameters were refined in separate series of least-squares cycles. Most sites were fully occupied within two standard deviations. The 16e silver site is only occupied by 94.8(2) %. In the final cycles this occupancy parameter was refined as a least-squares variable.

Table 1. Lattice parameters of  $R_4TMg$  compounds with cubic Gd<sub>4</sub>RhIn-type structure.

Compound	<i>a</i> (pm)	<i>V</i> (nm <sup>3</sup> )	Reference
<b>Palladium compounds</b>			
Ca <sub>4</sub> PdMg	1454.5(1)	3.0771	this work
Y <sub>4</sub> PdMg	1382.4(4)	2.6418	[11]
Sm <sub>4</sub> PdMg	1402.1(1)	2.7564	[11]
Eu <sub>4</sub> PdMg	1495.68(7)	3.3459	this work
Gd <sub>4</sub> PdMg	1389.5(3)	2.6827	[11]
Tb <sub>4</sub> PdMg	1378.6(1)	2.6201	this work
Dy <sub>4</sub> PdMg	1371.1(2)	2.5776	this work
Ho <sub>4</sub> PdMg	1366.5(1)	2.5517	this work
Er <sub>4</sub> PdMg	1363.4(2)	2.5344	this work
Tm <sub>4</sub> PdMg	1356.5(1)	2.4961	this work
Yb <sub>4</sub> PdMg	1434.6(1)	2.9525	this work
Lu <sub>4</sub> PdMg	1345.7(1)	2.4369	this work
<b>Silver compounds</b>			
Ca <sub>4</sub> AgMg	1485.78(7)	3.2780	this work
Yb <sub>4</sub> AgMg	1470.81(8)	3.1818	this work
<b>Platinum compounds</b>			
Y <sub>4</sub> PtMg	1380.11(8)	2.6287	[11]
Nd <sub>4</sub> PtMg	1405.6(2)	2.7771	[11]
Sm <sub>4</sub> PtMg	1396.5(4)	2.7235	[11]
Eu <sub>4</sub> PtMg	1483.95(9)	3.2678	this work
Gd <sub>4</sub> PtMg	1391.3(2)	2.6932	[11]
Tb <sub>4</sub> PtMg	1378.45(9)	2.6192	this work
Dy <sub>4</sub> PtMg	1373.6(5)	2.5917	this work
Ho <sub>4</sub> PtMg	1364.94(9)	2.5430	this work
Er <sub>4</sub> PtMg	1362.46(5)	2.5291	this work
Tm <sub>4</sub> PtMg	1357.5(1)	2.5016	this work
Yb <sub>4</sub> PtMg	1424.4(1)	2.8900	this work
Lu <sub>4</sub> PtMg	1349.0(1)	2.4549	this work
<b>Gold compounds</b>			
Ca <sub>4</sub> AuMg	1466.3(1)	3.1526	this work
Eu <sub>4</sub> AuMg	1515.6(1)	3.4814	this work
Yb <sub>4</sub> AuMg	1451.26(9)	3.0566	this work

Refinement of the correct absolute structure was ensured through calculation of the Flack parameter [17, 18]. The final difference Fourier synthesis revealed no residual peaks. The refined atomic positions, equivalent isotropic displacement parameters, and interatomic distances (exemplary for Ca<sub>4</sub>Ag<sub>0.948</sub>Mg) are given in Tables 3 and 4.

Further details of the crystal structure investigation may be obtained from Fachinformationszentrum Karlsruhe, 76344 Eggenstein-Leopoldshafen, Germany (fax: +49-7247-808-666; e-mail: crysdata@fiz-karlsruhe.de, [http://www.fiz-informationsdienste.de/en/DB/icsd/depot\\_anforderung.html](http://www.fiz-informationsdienste.de/en/DB/icsd/depot_anforderung.html)) on quoting the deposition number CSD-423920 (Ca<sub>4</sub>Ag<sub>0.948</sub>Mg) and CSD-423919 (Yb<sub>4</sub>PdMg).

#### Magnetic susceptibility measurements

Magnetic measurements were performed in the temperature range of 2.5–300 K using a Quantum Design Physical-Property-Measurement-System with magnetic flux densities up to 80 kOe. All measurements were carried out using the VSM option by packing the samples in kapton foil and at-

Table 2. Crystal data and structure refinement for Yb<sub>4</sub>PdMg and Ca<sub>4</sub>Ag<sub>0.948(2)</sub>Mg, space group  $F\bar{4}3m$ ,  $Z = 16$ .

Empirical formula	Yb <sub>4</sub> PdMg	Ca <sub>4</sub> Ag <sub>0.948</sub> Mg
Formula weight, g mol <sup>-1</sup>	822.87	286.84
Unit cell dimension (Guinier powder data):		
<i>a</i> , pm	1434.6(1)	1485.78(7)
Cell volume <i>V</i> , nm <sup>3</sup>	2.9525	3.2799
Calculated density, g cm <sup>-3</sup>	7.41	2.32
Crystal size, μm <sup>3</sup>	5 × 25 × 45	60 × 160 × 220
Transmission ratio (min / max)	0.249 / 0.700	0.494 / 0.834
Absorption coefficient, mm <sup>-1</sup>	52.5	4.80
<i>F</i> (000), e	5408	2185
Detector distance, mm	70	80
Exposure time, min	5	6
$\omega$ range; increment, deg	0–180; 1	0–180; 1
Integration params A; B; EMS	12.8; 2.8; 0.012	13.2; 3.0; 0.013
$\theta$ range for data collection, deg	2–31	2–32
Range in <i>hkl</i>	±22, ±22, ±22	±22, ±22, ±22
Total no. of reflections	8930	9739
Independent reflections / <i>R</i> <sub>int</sub>	523 / 0.0643	617 / 0.0201
Reflections with $I \geq 2\sigma(I)$ / <i>R</i> <sub>σ</sub>	467 / 0.0433	607 / 0.0093
Data / parameters	523 / 18	617 / 20
<i>R</i> 1 / <i>wR</i> 2 for $I \geq 2\sigma(I)$	0.0397 / 0.0259	0.0097 / 0.0186
<i>R</i> 1 / <i>wR</i> 2 for all data	0.0484 / 0.0269	0.0106 / 0.0188
Goodness-of-fit on <i>F</i> <sup>2</sup>	0.999	1.105
Extinction coefficient	—	0.00024(2)
Flack parameter	0.01(3)	0.05(3)
Largest diff. peak / hole, e Å <sup>-3</sup>	3.62 / -2.85	0.25 / -0.26

Table 3. Atomic coordinates and anisotropic displacement parameters (pm<sup>2</sup>) for Ca<sub>4</sub>Ag<sub>0.948(2)</sub>Mg and Yb<sub>4</sub>PdMg. *U*<sub>eq</sub> is defined as one third of the trace of the orthogonalized *U*<sub>ij</sub> tensor.

Atom	Site	<i>x</i>	<i>y</i>	<i>z</i>	<i>U</i> <sub>eq</sub>
<b>Ca<sub>4</sub>Ag<sub>0.948(2)</sub>Mg</b>					
Ca1	24g	0.43879(3)	3/4	3/4	242(1)
Ca2	24f	0.80626(3)	0	0	228(1)
Ca3	16e	0.64939(2)	<i>x</i>	<i>x</i>	238(1)
Ag <sup>a</sup>	16e	0.85784(1)	<i>x</i>	<i>x</i>	262(1)
Mg	16e	0.42186(3)	<i>x</i>	<i>x</i>	222(2)
<b>Yb<sub>4</sub>PdMg</b>					
Yb1	24g	0.44271(8)	3/4	3/4	212(2)
Yb2	24f	0.80789(7)	0	0	172(1)
Yb3	16e	0.65469(5)	<i>x</i>	<i>x</i>	153(2)
Pd	16e	0.85984(7)	<i>x</i>	<i>x</i>	207(2)
Mg	16e	0.4222(3)	<i>x</i>	<i>x</i>	161(19)

<sup>a</sup> The silver site is occupied by 94.8(2) %.

taching them to a brass sample holder. For these measurements 15.891 mg of Eu<sub>4</sub>PdMg and 7.662 mg of Eu<sub>4</sub>PtMg were used.

#### Electronic structure calculations

The most appropriate theoretical framework for examining the electronic structure and related properties such as the chemical bonding is the density functional theory (DFT) [19, 20]. Within DFT we use the full potential scalar-relativistic augmented spherical wave (ASW) method

Table 4. Interatomic distances (pm), for  $\text{Ca}_4\text{Ag}_{0.948}(2)\text{Mg}$  calculated with the powder lattice parameters. Standard deviations are equal or smaller than 0.1 pm. All distances of the first coordination spheres are listed.

Ca1:	2	Mg	362.0	Ca3:	3	Ag	310.1
	2	Ca3	377.6		3	Mg	369.7
	2	Ag	377.7		3	Ca1	377.6
	4	Ca2	391.4		3	Ca2	391.0
Ca2:	4	Ca1	396.7	Ag:	3	Ca3	422.8
	2	Ag	308.4		3	Ca2	308.4
	2	Mg	376.6		3	Ca3	310.1
	2	Ca3	391.0		3	Ca1	377.7
Mg:	4	Ca1	391.4	Mg:	3	Mg	328.4
	4	Ca2	407.1		3	Ca1	362.0
					3	Ca3	369.7
					3	Ca2	376.6

[21, 22] which has shown its reliability in treating the electronic structure and bonding properties of intermetallic compounds [23, and refs. therein]. Exchange and correlation effects are accounted for with the generalized gradient approximation GGA following the scheme of Perdew, Burke and Ernzerhof [24]. In the ASW method, the wave function is expanded in atom-centered augmented spherical waves, which are Hankel functions and numerical solutions of the Schrödinger equation, respectively, outside and inside the so-called augmentation spheres. In the minimal ASW basis set, we chose the outermost shells to represent the valence states, and the matrix elements were constructed using partial waves up to  $l_{\max} + 1 = 3$  for all atomic constituents ( $l$ : secondary quantum number). Self-consistency was achieved when charge transfers and energy changes between two successive cycles were such as:  $\Delta Q < 10^{-8}$  and  $\Delta E < 10^{-6}$  eV, respectively. The Brillouin zone integrations were performed using the linear tetrahedron method within the irreducible wedge following Blöchl [25]. The calculations are carried out assuming spin degenerate configuration and neutral atoms with their multiplicities (Table 3). Besides the site projected density of states (PDOS), we discuss qualitatively the pair interactions based on the covalent bond energy (ECOV) criterion which uses both the overlap and the Hamiltonian populations [26]. In the plots negative, positive and zero ECOV magnitudes indicate bonding, anti-bonding, and non-bonding interactions, respectively.

## Discussion

### Crystal chemistry

The series of rare earth element-rich compounds  $\text{RE}_4\text{PdMg}$  and  $\text{RE}_4\text{PtMg}$  have been completed. The palladium-based series starts from the samarium compound on, while  $\text{Nd}_4\text{PtMg}$  is the representative with the largest rare earth element for the platinum series. The yttrium compounds of both series fit in be-

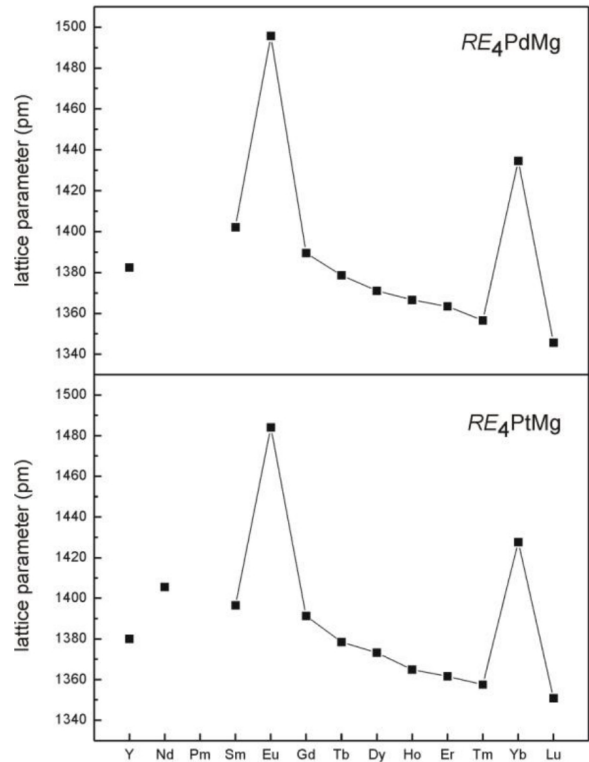


Fig. 1. Course of the lattice parameters of the cubic compounds  $\text{RE}_4\text{PdMg}$  and  $\text{RE}_4\text{PtMg}$ .

tween the gadolinium and terbium compounds. The cell volumes decrease with increasing atomic number of the rare earth element (lanthanide contraction; Fig. 1) with the exception of the europium and ytterbium compounds. Here, for the first time, it was possible to synthesize  $\text{Gd}_4\text{RhIn}$ -type compounds with a divalent rare earth element. The strong positive deviations of these compounds from the smooth Landelli plot are indicative of stable  $4f^7$  and  $4f^{14}$  configurations. The divalent character of europium has experimentally been proven by magnetic susceptibility measurements (*vide infra*). Motivated by these results we tested other element combinations and obtained also the ternary phases  $\text{Yb}_4\text{AgMg}$ ,  $\text{Eu}_4\text{AuMg}$ , and  $\text{Yb}_4\text{AuMg}$ , as well as the calcium compounds  $\text{Ca}_4\text{TMg}$  ( $T = \text{Pd}, \text{Ag}, \text{Au}$ ). In total we obtained 20 new representatives of the  $\text{Gd}_4\text{RhIn}$  type.

Since a high-quality data set was refined for  $\text{Ca}_4\text{Ag}_{0.948}\text{Mg}$ , the following discussion relies on this compound. The crystal chemistry and chemical bonding of  $\text{Gd}_4\text{RhIn}$ -type compounds has repeatedly been discussed [5, 6 and refs. therein]. Herein we focus on

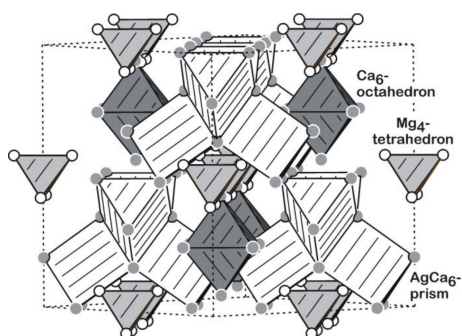


Fig. 2. Cutout of the cubic  $\text{Ca}_4\text{AgMg}$  structure. The characteristic building units of  $\text{AgCa}_6$  trigonal prisms, empty  $\text{Ca}_6$  octahedra and  $\text{Mg}_4$  tetrahedra are emphasized.

the new features.  $\text{Ca}_4\text{Ag}_{0.948}\text{Mg}$  is the first alkaline earth metal compound with this structure type, and we observe a clear segregation of the magnesium and calcium atoms into two different substructures. As is emphasized in the cut-out of Fig. 2, the calcium atoms take part in two structural motifs, *i. e.* silver-centered trigonal prisms  $\text{AgCa}_6$  and empty  $\text{Ca}_6$  octahedra. The  $\text{AgCa}_6$  prisms are condensed *via* common corners and edges to a three-dimensional adamantane-related network. The cavities generated by this network are filled by the  $\text{Ca}_6$  octahedra and the  $\text{Mg}_4$  tetrahedra.

The crystal chemical behavior of calcium and magnesium in  $\text{Ca}_4\text{Ag}_{0.948}\text{Mg}$  nicely underlines the different chemical potentials. Calcium occupies the positions typical for an electropositive element, while magnesium takes the position of the *p* element, forming the covalently bonded tetrahedra, similar to aluminum [4] and indium [1, 2, 4]. Such segregation has already been observed for  $\text{In}_4$  tetrahedra in alkaline earth nitride matrices of  $(\text{A}_{19}\text{N}_7)[\text{In}_4]_2$  ( $\text{A} = \text{Ca}, \text{Sr}$ ) [27] and  $\text{A}_6\text{In}_4(\text{In}_x\text{Li}_y)\text{N}_{3-z}$  ( $\text{A} = \text{Sr}, \text{Ba}$ ) [28]. For magnesium such tetrahedra had first been reported as aggregates in noble gas matrices [29, 30]. The predicted distance of 301 pm for tetramagnesium [30], however, is much shorter than the one of 328 pm observed for  $\text{Ca}_4\text{Ag}_{0.948}\text{Mg}$  and the other  $\text{RE}_4\text{TMg}$  intermetallics [5].

The Ca–Ag distances in the prismatic network of 308 and 310 pm compare well with the sum of the covalent radii [12] of 308 pm, underlining the strong covalent Ca–Ag bonding. Within the  $\text{Ca}_6$  octahedra as well as between the  $\text{AgCa}_6$  prisms and the  $\text{Ca}_6$  octahedra we observe a broad range of Ca–Ca distances, *i. e.* 378–423 pm. The shorter ones are shorter than in *fcc* calcium 395 pm [31].

Finally we turn back to the VEC and the stability range of  $\text{RE}_4\text{TX}$  intermetallics. The highest VEC of 25 per *f. u.* (*f. u.* = formula unit) has been observed for  $\text{Ce}_4\text{RuIn}$  [4] which contains intermediate-valent cerium with an average formal oxidation state of +3.5. The synthesis of  $\text{Ca}_4\text{PdMg}$  reported herein led to the 4-1-1 compound with the so far lowest VEC of 20. Further variation of the *T* and *X* components will lead to new  $\text{RE}_4\text{TX}$  compounds. Systematic phase analytical work is in progress.

### Electronic structure and chemical bonding

The site projected density of states (PDOS) of  $\text{Ca}_4\text{AgMg}$  is shown in Fig. 3. For the sake of comparison we also exhibit the PDOS for  $\text{Ca}_4\text{PdMg}$ . Site multiplicities (Table 3) are accounted for in the plots. In both panels the energy reference along the *x* axis is

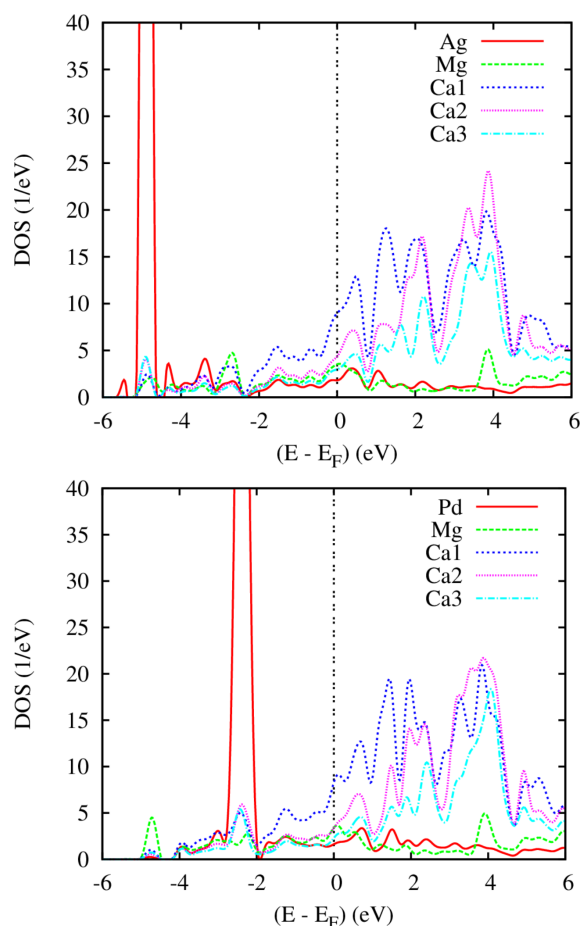


Fig. 3 (color online). Site projected density of states (PDOS) for  $\text{Ca}_4\text{AgMg}$  (top) and  $\text{Ca}_4\text{PdMg}$  (bottom).

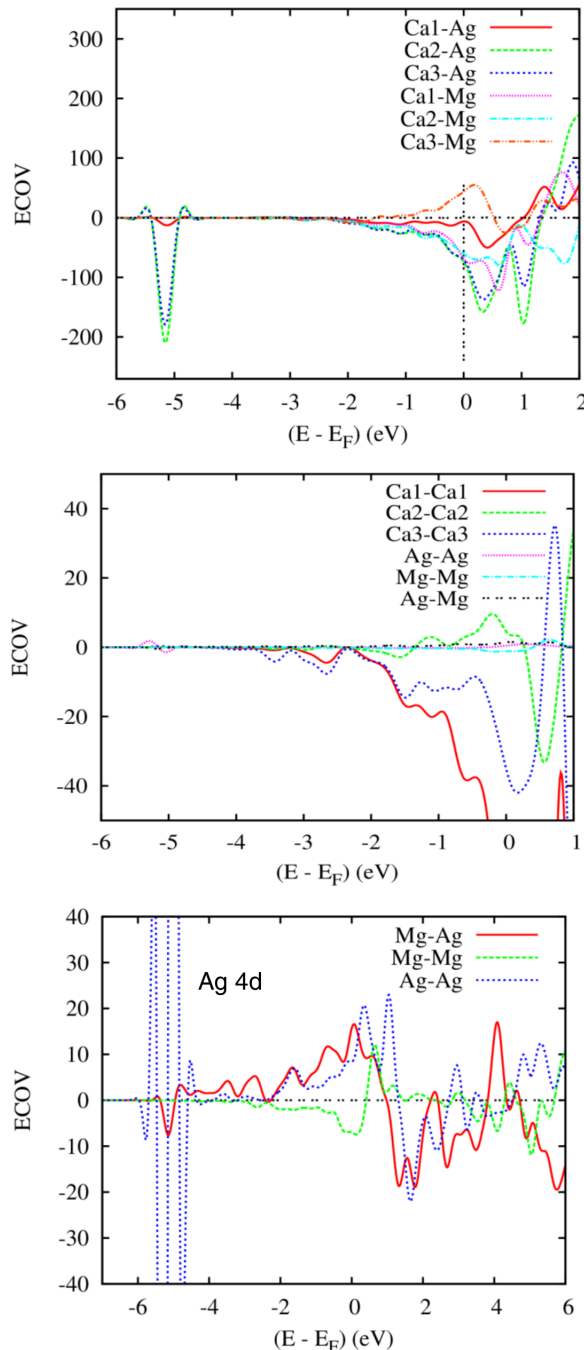


Fig. 4 (color online). Chemical bonding properties from ECOV (covalent bond energy criterion) in  $\text{Ca}_4\text{AgMg}$ . The lower panel shows other interactions of low intensity involving all sites multiplicities.

with respect to the Fermi level ( $E_F$ ) which crosses a finite broad PDOS of all constituents, with the largest

contribution arising from calcium, namely Ca1 and Ca2 due to their higher Wyckoff multiplicity in the structure (Table 3). Both compounds are metallic with  $s$ -like conductivity. The PDOS of all constituents have similar shapes, indicating quantum mixing between the valence states. Contrary to the  $s$ -like dispersive states (broad) crossing  $E_F$ , the largely filled  $4d$  states, considered in the valence basis set for both Ag and Pd in the calculations, exhibit localized and large peak intensities within the valence band (VB) with a lower lying Ag( $4d$ ) PDOS at  $\sim -5$  eV as compared to Pd( $4d$ ) at  $\sim -2$  eV due to the surplus electron, *i. e.* Ag ( $Z = 47$ ) vs. Pd ( $Z = 46$ ). Despite the high filling of the  $d$  states, there are significant contributions under the  $d$  PDOS arising mainly from calcium. This result signals quantum mixing between them as discussed below. The empty conduction band (CB) is dominated by calcium states (Ca1, Ca2, Ca3) and less so by states of Mg and Ag (Pd). In spite of the large number of Ca atoms and their site multiplicities which result in larger intensity PDOS, it can be assumed that there is charge transfer from calcium towards Mg and Ag (Pd). This may follow from the trends of the Pauling electronegativities [12]:  $\chi(\text{Ca}) = 1.00$ ;  $\chi(\text{Mg}) = 1.31$ ;  $\chi(\text{Ag}) = 1.93$  and  $\chi(\text{Pd}) = 2.20$  whereby calcium is the most electropositive element. Nevertheless bonding in the compounds is described as covalent.

Focussing on  $\text{Ca}_4\text{AgMg}$ , Fig. 4 shows the plot of the ECOV (unitless) accounting for one atomic species of each kind. There are two main bonding regions:  $\{-5.5, 5 \text{ eV}\}$  for the Ca–Ag interactions and  $\{-2, E_F\}$  for the other interactions. The bonding between Ag and Ca in the lower energy part involves Ag ( $4d$ ) with mainly Ca2 and Ca3. This is in agreement with the course of the distances (Table 4) and with the dominating  $\text{AgCa}_6$  prisms formed by Ca2 and Ca3. The Ca1 atoms at the much longer Ca1–Ag distance of 378 pm show a much weaker ECOV contribution. The other region of bonding ranging from below  $E_F$  involves the bonding of Ca with similar intensity ratios, *i. e.*, little contribution from Ca1 as compared to Ca2 and Ca3. Ca–Mg bonding is also present with similar intensity. The Ca3–Mg interaction is weakly antibonding, but compensated by a bonding Ca3–Ag contribution in the same energy range.

Fig. 4 (middle) shows the ECOV for pair interactions in species of the same kind, detailing the three Ca–Ca bonds. These are found dominant as compared to all other bonds such as Ag–Ag and Mg–Mg. This

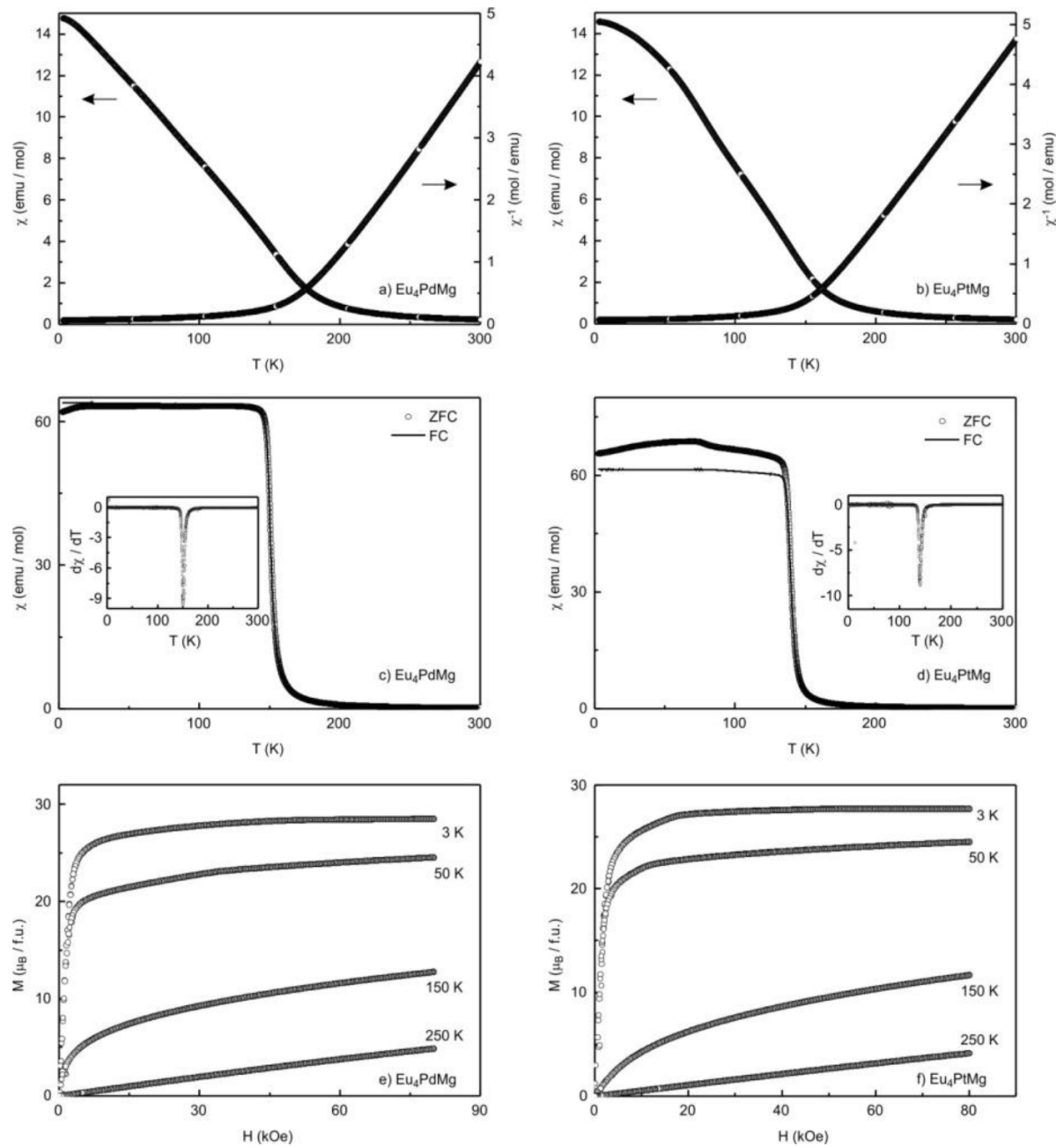


Fig. 5. Temperature dependence of the susceptibility and inverse susceptibility ( $\chi$  and  $\chi^{-1}$  data) measured at an applied field of 10 kOe of a)  $\text{Eu}_4\text{PdMg}$  and b)  $\text{Eu}_4\text{PtMg}$ ; c) and d) temperature dependence of the magnetic susceptibility measured in zero-field-cooled/field-cooled mode with an applied field of 100 Oe of  $\text{Eu}_4\text{PdMg}$  and  $\text{Eu}_4\text{PtMg}$  respectively, insets depict the first derivative of  $\chi$  with respect to  $T$  plotted vs.  $T$ ; e) and f) magnetization isotherms measured at 3, 50, 150 and 250 K of  $\text{Eu}_4\text{PdMg}$  and  $\text{Eu}_4\text{PtMg}$ .

is further shown in the lower panel of Fig. 4 with an account of site multiplicities (all four atoms). The Mg–Mg interaction is mainly of bonding character

(negative ECOV) and gives a signature of the  $\text{Mg}_4$  tetrahedra. On the contrary, Ag–Ag and Ag–Mg are found antibonding throughout the VB (positive ECOV



intensities). While the half bonding/half antibonding Ag  $d$ - $d$  interaction does not influence the stability of the compound, the weak antibonding chemical interactions involving Ag within  $\text{Ca}_4\text{AgMg}$  are destabilizing and might be the reason for the small silver defects in the  $\text{Ca}_4\text{Ag}_{0.948}\text{Mg}$  structure.

#### Magnetic properties of $\text{Eu}_4\text{PdMg}$ and $\text{Eu}_4\text{PtMg}$

The temperature dependence of the susceptibilities and inverse susceptibilities ( $\chi$  and  $\chi^{-1}$  data) of  $\text{Eu}_4\text{PdMg}$  and  $\text{Eu}_4\text{PtMg}$ , measured at an applied field of 10 kOe, is displayed in Figs. 5 a) and b), respectively. Both compounds show drastic increases of the susceptibilities below 200 K indicating the beginning of their magnetic ordering.

In the case of  $\text{Eu}_4\text{PdMg}$  we were able to fit the inverse susceptibility data with the Curie-Weiss law in the temperature range of 230–300 K yielding an effective magnetic moment of  $\mu_{\text{eff}} = 7.94(1) \mu_{\text{B}}$  per Eu atom and a paramagnetic Curie constant of  $\theta_{\text{p}} = 167(1)$  K, the first being consistent with the spin-only, free-ion value for  $\text{Eu}^{2+}$  ions and the latter indicating ferromagnetic interactions in the paramagnetic region. In case of  $\text{Eu}_4\text{PtMg}$  it was possible to fit the inverse susceptibility data with the Curie-Weiss law in the temperature range of 200–300 K resulting in  $\mu_{\text{eff}} = 8.00(1) \mu_{\text{B}}$  per Eu atom and  $\theta_{\text{p}} = 148(1)$  K.

In order to determine the correct ordering temperatures, measurements in *zero-field-cooled/field-cooled* mode were carried out at an applied field of 100 Oe. The temperature dependence of the susceptibilities of these measurements is displayed in Figs. 5 c) and d) for

$\text{Eu}_4\text{PdMg}$  and  $\text{Eu}_4\text{PtMg}$ , respectively. The ferromagnetic ordering takes place at  $T_{\text{C}} = 150.1(5)$  K for the Pd and at  $T_{\text{C}} = 139.1(5)$  K for the Pt compound. These temperatures were obtained by plotting  $d\chi/dT$  vs.  $T$  [insets Figs. 5 c) and d)]. In the case of  $\text{Eu}_4\text{PtMg}$  it is clearly visible that the ZFC curve deviates from the FC curve below the ferromagnetic ordering temperature, and that the ZFC curve exhibits a minor anomaly (Fig. 5d). This anomaly is found to be at approximately 77 K, close to the ferromagnetic ordering temperature of EuO.

Figs. 5 e) and f) show the magnetization isotherms measured at 3, 50, 150, and 250 K. In both cases the magnetization isotherm at 250 K exhibits a linear increase with the applied field as expected for paramagnetic materials.

The magnetization isotherms observed below the magnetic ordering temperature follow the course expected for ferromagnetic materials. The isotherms show a drastic increase of the magnetization at small fields and approach saturation magnetization asymptotically above an applied field of 10 kOe. The 3 K isotherms of  $\text{Eu}_4\text{PdMg}$  and  $\text{Eu}_4\text{PtMg}$  exhibit saturation magnetizations ( $m$ ) of  $\mu_{\text{exp}(m)} = 7.13(1)$  and  $6.93(1) \mu_{\text{B}}$  per Eu atom, respectively, in good agreement with the theoretical value according to  $g_{\text{J}} \times J = 7 \mu_{\text{B}}$  per  $\text{Eu}^{2+}$  ion. There was also no apparent hysteresis, so the compounds appear to be soft ferromagnets.

#### Acknowledgement

This work was supported by the Deutsche Forschungsgemeinschaft.

- 
- [1] R. Zaremba, U.Ch. Rodewald, R.-D. Hoffmann, R. Pöttgen, *Monatsh. Chem.* **2007**, 138, 523.
  - [2] R. Zaremba, U.Ch. Rodewald, R.-D. Hoffmann, R. Pöttgen, *Monatsh. Chem.* **2008**, 139, 481.
  - [3] Zh. M. Kurenbaeva, E. V. Murashova, D. N. Hannanov, A. B. Ilyukin, A. I. Tursina, Yu. D. Seropegin, *XI International Conference on Crystal Chemistry of Intermetallic Compounds*, Lviv, Ukraine, **2010**, P61.
  - [4] F. Tappe, C. Schwickert, S. Linsinger, R. Pöttgen, *Monatsh. Chem.* **2011**, 142, 1087.
  - [5] U. Ch. Rodewald, B. Chevalier, R. Pöttgen, *J. Solid State Chem.* **2007**, 180, 1720.
  - [6] F. Tappe, R. Pöttgen, *Rev. Inorg. Chem.* **2011**, 31, 5.
  - [7] R. Pöttgen, R.-D. Hoffmann, *Metall* **2004**, 58, 722.
  - [8] S. Tuncel, J.G. Roqufère, C. Stan, J.-L. Bobet, B. Chevalier, E. Gaudin, R.-D. Hoffmann, U. Ch. Rodewald, R. Pöttgen, *J. Solid State Chem.* **2009**, 182, 229.
  - [9] W. Hermes, U.Ch. Rodewald, R. Pöttgen, *J. Appl. Phys.* **2010**, 108, 113919.
  - [10] S. Linsinger, W. Hermes, B. Chevalier, S. Couillaud, J.-L. Bobet, M. Eul, R. Pöttgen, *Intermetallics* **2009**, 17, 1028.
  - [11] S. Tuncel, B. Chevalier, R. Pöttgen, *Z. Naturforsch.* **2008**, 63b, 600.
  - [12] J. Emsley, *The Elements*, Oxford University Press, Oxford **1999**.
  - [13] R. Pöttgen, Th. Gulden, A. Simon, *GIT Labor-Fachzeitschrift* **1999**, 43, 133.
  - [14] R. Pöttgen, A. Lang, R.-D. Hoffmann, B. Künnen,



- G. Kotzyba, R. Müllmann, B. D. Mosel, C. Rosenhahn, *Z. Kristallogr.* **1999**, 214, 143.
- [15] K. Yvon, W. Jeitschko, E. Parthé, *J. Appl. Crystallogr.* **1977**, 10, 73.
- [16] G. M. Sheldrick, SHELXL-97, Program for the Refinement of Crystal Structures, University of Göttingen, Göttingen (Germany) **1997**. See also: G. M. Sheldrick, *Acta Crystallogr.* **2008**, A64, 112.
- [17] H. D. Flack, G. Bernadinelli, *Acta Crystallogr.* **1999**, A55, 908.
- [18] H. D. Flack, G. Bernadinelli, *J. Appl. Crystallogr.* **2000**, 33, 1143.
- [19] P. Hohenberg, W. Kohn, *Phys. Rev.* **1964**, 136, B864.
- [20] W. Kohn, L. J. Sham, *Phys. Rev.* **1965**, 140, A1133.
- [21] A. R. Williams, J. Kübler, C. D. Gelatt, Jr., *Phys. Rev. B* **1979**, 19, 6094.
- [22] V. Eyert, *The Augmented Spherical Wave Method - A Comprehensive Treatment, Lecture Notes in Physics*, Vol. 719, Springer, Berlin, Heidelberg, **2007**.
- [23] S. F. Matar, J. F. Riecken, B. Chevalier, R. Pöttgen, A. F. Al Alam, V. Eyert *Phys. Rev. B* **2007**, 76, 174434.
- [24] J. Perdew, K. Burke, M. Ernzerhof, *Phys. Rev. Lett.* **1996**, 77, 3865.
- [25] P. E. Blöchl, *Phys. Rev. B* **1994**, 50, 17953.
- [26] G. Bester, M. Fähnle, *J. Phys.: Condens. Matter* **2001**, 13, 11541.
- [27] M. Kirchner, W. Schnelle, F. R. Wagner, R. Kniep, R. Niewa, *Z. Anorg. Allg. Chem.* **2005**, 631, 1477.
- [28] M. S. Bailey, D. Y. Shen, M. A. McGuire, D. C. Fredrickson, B. H. Toby, F. J. DiSalvo, H. Yamane, S. Sasaki, M. Shimada, *Inorg. Chem.* **2005**, 44, 6680.
- [29] J. C. Miller, R. L. Mowery, E. R. Krausz, S. M. Jacobs, H. W. Kim, P. N. Schatz, L. Andrews, *J. Chem. Phys.* **1981**, 74, 6349.
- [30] A. Kaufmann, A. Kornath, A. Zoermer, R. Ludwig, *Inorg. Chem.* **2010**, 49, 3851.
- [31] J. Donohue, *The Structures of the Elements*, Wiley, New York **1974**.